Available online at www.sciencedirect.com
ScienceDirect
Trans. Nonferrous Met. Soc. China 35(2025) 3734−3750
Transactions of Nonferrous Metals Society of China
www.tnmsc.cn

Microstructural evolution, mechanical properties and corrosion resistance of Ti−12Ni alloy fabricated by laser powder bed fusion

Kai HUANG[1], Yao-jia REN[1], Qing-ge WANG[1], Yi LIU[2], Quan FU[2], Ning LI[3], Ian BAKER[4], Min SONG[1], Hong WU[1]

1. State Key Laboratory of Powder Metallurgy, Central South University, Changsha 410083, China;
2. Yunnan Precious Metals Laboratory Co., Ltd., Kunming 650106, China;
3. Department of Oral and Maxillofacial Surgery, Center of Stomatology, Xiangya Hospital, Central South University, Changsha 410008, China;
4. Thayer School of Engineering, Dartmouth College, Hanover, NH 03755, USA

Received 25 February 2024; accepted 30 October 2024

Abstract: The microstructural evolution, mechanical properties, and corrosion behavior of Ti−12Ni (wt.%) specimens produced by laser powder bed fusion (LPBF) using various volume energy density (VED) processing parameter values were investigated. The results showed that the alloy prepared at a low VED of 67 J/mm^3 consisted of near-β grains. At a VED of 133 J/mm^3, the alloy exhibited coarse primary Ti_2Ni and fine eutectoid structure. This eutectoid structure consisted of α laths and two types of nanoscale Ti_2Ni, one in the form of short rods and the other with a spherical morphology. Further increase of the VED to 267 J/mm^3 led to coarsening of the eutectoid structure. The dispersed Ti_2Ni nanoparticles exhibited a significant strengthening effect. The alloy produced at a VED of 133 J/mm^3 showed the greatest strength with a nanohardness of (7.8±0.1) GPa and a compressive strength of (1777±27) MPa. However, the presence of Ni segregation and holes produced by the LPBF processing adversely affected the corrosion resistance of the alloy.

Key words: Ti−12Ni alloy; laser powder bed fusion; microstructural evolution; mechanical properties; corrosion resistance

1 Introduction

Titanium alloys are good candidates for applications in the biomedical, aerospace, and automotive fields due to their high specific strength, excellent biocompatibility, and corrosion resistance [1]. Traditional methods for preparing titanium alloys include casting, forging, and powder metallurgy, which are time consuming and can only produce relatively simple structural parts [2,3]. Unfortunately, the high cost and poor machinability seriously limit the engineering applications of titanium alloys [4,5]. Recently, laser powder bed fusion (LPBF), an additive manufacturing (AM) method, has developed rapidly and become quite mature [5]. It is an advanced manufacturing technology that uses computer-aided methods for rapid prototyping, which overcomes the limitations of conventional tools and dies. In LPBF processing, fluid metal powders are melted and stacked layer-by-layer to form parts [6]. It can be used to manufacture products with complex structures, and stimulate new ways for the development and manufacture of titanium alloys [7]. Several titanium alloys have been processed by LPBF, including Ti−6Al−4V, Ti−24Nb−4Zr−8Sn and Ti−6Al−2V−1.5Mo−0.5Zr−0.3Si [8−10].

Corresponding author: Hong WU, Tel: +86-731-88836296, E-mail: wuhong927@126.com
https://doi.org/10.1016/S1003-6326(25)66909-3

For AM titanium alloys, the microstructure is typically composed of coarse columnar dendrites containing solidification defects and exhibiting anisotropic mechanical properties [5,11]. Therefore, the columnar-to-equiaxed transition (CET) is considered an important problem to be investigated in such alloys [12]. In recent years, many efforts have been made to refine the grains of titanium alloys [13,14]. By adding La_2O_3 particles as grain refiners to promote heterogeneous nucleation, CHEN et al [15] achieved significant refinement of the prior β grains. ZHANG et al [16] used laser metal deposition (LMD) to make a Ti−Cu alloy with fully-equiaxed β grains and an ultra-fine eutectoid structure by mixing it with different amounts of copper. A large growth restriction factor Q ($=c_0 \cdot Q_n$) (c_0 is the solubility in β titanium; Q_n is the normalized Q value) and rapid diffusion in titanium of eutectoid-forming elements are anticipated to generate a very fine eutectoid microstructure. Nickel is a typical eutectoid-forming element in titanium. It has a maximum solubility of 12.5 wt.% in β titanium, and a value of Q_n of 14.3 K, which is higher than that of Cu (6.5 K) [17]. As a result, the maximum growth limiting factor $Q_{max}=c_{max} \cdot Q_n=178.8$ K (c_{max} is the maximum solubility in β titanium). XIONG et al [18] used LPBF to prepare Ti−Ni alloys with Ni contents of 3, 1.6, and 0.4 wt.%, and found the beneficial effect of Ni on the grain refinement and strengthening of additively manufactured titanium alloys. Recently, XUE et al [19] added 3 wt.% Ni for direct energy deposition (DED) of Ti−6Al−4V, and obtained fine, equiaxed prior-β grains. NARAYANA et al [20] added 5 wt.% Ni to Ti and prepared a Ti−5Ni alloy by DED, which had excellent mechanical properties.

According to the conventional view, the addition of Ni will result in the formation of the brittle intermediate phase Ti_2Ni, which will likely have a detrimental effect on the properties of a titanium alloy [18]. Nevertheless, recent studies have indicated that Ti_2Ni may also exert a beneficial influence. LI et al [21] reported that a reduction in Ti_2Ni resulted in a decline in the load-bearing capacity of TiNi-based structural parts. LU et al [22] found that the precipitation of nano-scale spherical Ti_2Ni could enhance the tensile strength and shape memory properties of TiNi alloys. Using inter-metallic phases to achieve the optimum balance of properties is an issue worth investigating for Ti−Ni alloys. When the Ni content exceeds 10 wt.%, both a coarse Ti_2Ni phase and a lamellar mixture of α-Ti and Ti_2Ni are present in the Ti−Ni alloy [23]. In order to investigate the impact of various forms of Ti_2Ni on additive manufacturing of Ti−Ni alloys, Ti−12Ni (wt.%) was selected for research.

Multiple parameters control LPBF processing [24,25]. Current best practices use an empirical metric known as the volumetric energy density (VED), which is the energy per unit volume supplied to the powder bed and is closely linked to process performance. The VED is defined as follows:

$$\mathrm{VED}=P/(vth) \tag{1}$$

where P, v, t, and h are the laser power, the scanning speed, the layer thickness, and the hatch spacing, respectively [26,27]. Previous studies showed that the VED significantly impacted the precipitation behavior of the intermediate phase in Ti−Ni alloys produced via LPBF. LU et al [28] observed that a TiNi shape memory alloy produced by LPBF was more conducive to the precipitation of nanoscale Ti_2Ni at a relatively low energy density than conventionally produced alloys. GU et al [29] demonstrated that the Ni_4Ti_3 phase precipitated from LPBF-produced NiTi-based composites, resulting in a nanostructure at a relatively low VED. As the VED increased, the Ni_4Ti_3 phase became coarser. Thus, VED is an effective factor that regulates the morphologies of Ti−Ni alloys prepared by LPBF.

In this work, Ti−12Ni specimens were prepared by LPBF at various laser powers and scanning speeds. The effects of different VEDs on the formability, phase composition, and microstructural evolution were investigated. The relationship between the microstructure and properties, including the nanoindentation behavior and corrosion properties of the specimens, was analyzed and discussed in detail.

2 Experimental

A blended powder mixture of Ti−12Ni was prepared by mixing high-purity (>99.9%) titanium and nickel powders at a mass ratio of 88∶12 in a cylindrical tube rotated at 80 r/min for 12 h (see Figs. 1(a, b)). The particle size distribution is shown

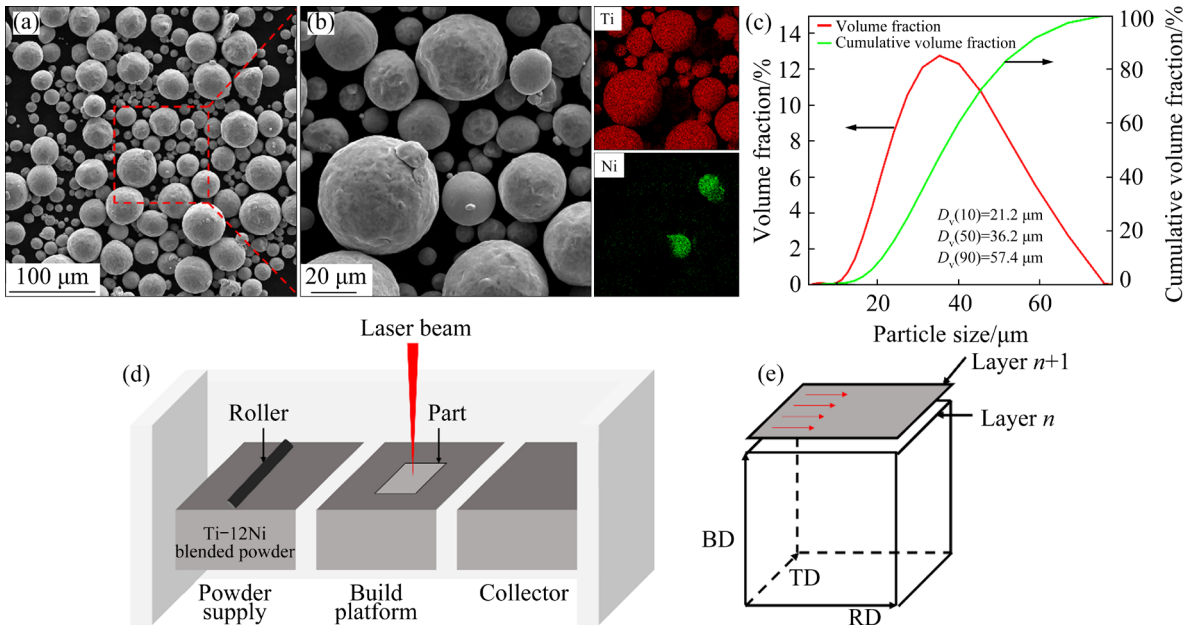

Fig. 1 (a, b) Secondary electron images showing Ti−12Ni powder morphology and corresponding EDS maps; (c) Powder particle size distribution; (d) Schematic of LPBF process; (e) Schematic of scanning strategy

in Fig. 1(c): $D_v(10)$=21.2 μm, $D_v(50)$=36.2 μm, and $D_v(90)$= 57.4 μm. To fabricate specimens, a Farsoon FS 121 LPBF machine outfitted with a 500 W, 60 μm spot fiber laser was used. The h and t were held at 80 and 30 μm, respectively. Different processing parameters were achieved by varying the v (500−1000 mm/s) and P (160−320 W). Specimens were produced at VEDs of 67−267 J/mm^3. The oxygen level in the printing chamber was maintained to be less than 0.01% (mass fraction) via introducing high-purity argon gas. The scanning direction was rotated 67° between layers. Figure 1(d) depicts a schematic of the LPBF process, and Fig. 1(e) illustrates the scanning strategy employed.

X-ray diffraction (XRD) using Cu K_α radiation was employed to identify the phases present. The diffraction angle (2θ) spanned from 20° to 90°, in steps of 0.02°. The specimens underwent grinding, polishing, and then etching with Kroll's reagent (5 vol.% HF, 15 vol.% HNO_3 and 80 vol.% H_2O) for 15 s. The segregation behavior of the as-built specimens was characterized using an electron probe micro-analyzer (EPMA, JXA−8230, JOEL). The microstructures were observed using an FEI Quanta FEG250 scanning electron microscope (SEM) operated at 18 kV, which is equipped with X-ray energy dispersive spectroscopy (EDS) and electron backscatter diffraction (EBSD) detectors. Before conducting EBSD acquisition, ion polishing was carried out to alleviate stresses and ensure a polished specimen surface. EBSD examinations were performed at an operating voltage of 18 kV and a step size of 0.035 μm. The EBSD data were analyzed using AZtecCrystal software. To obtain detailed microstructural information, specimens were extracted from specific regions and analyzed using an FEI Talos F200X transmission electron microscope (TEM) operated at 300 kV. Thin slices were first ground to ~50 μm in thickness and then twin-jet electropolished using a solution consisting of 60 vol.% methanol, 35 vol.% butanol, and 5 vol.% perchloric acid at −20 °C and 30 V.

The Archimedes method was used to evaluate the density of specimens. A GSM nano-indenter was used to perform nanoindentation tests with a maximum indentation load of 30 mN and a duration of 15 s. Compression tests were conducted using an Instron−8802 machine at an initial strain rate of 1×10^{-3} s^{-1}. Cylindrical specimens with a diameter of 4 mm and a height of 6 mm were cut parallel to the BD direction. A CS electrochemical workstation was used for electrochemical measurements, which had a three-electrode cell consisting of a saturated glycerol electrode (SCE) as the reference electrode, test specimens as the working electrode, and a platinum sheet as the counter electrode. The measurements were carried out in 3.5 wt.% NaCl solutions at room temperature. Before testing, specimens were ground and polished following standard procedures, then cleaned using deionized

water and ethanol under ultrasonic conditions, and finally dried in air. The system was on standby for 30 min before each measurement. The open circuit potential (OCP) was measured, followed by potentiodynamic polarization testing. Polarization curves were collected in the potential range from −0.5 to 2.5 V relative to the OCP (vs SCE) at a scanning rate of 1 mV/s.

3 Results

3.1 Formability

Figure 2(a) shows the densities of the Ti−12Ni specimens formed by LPBF under different processing conditions. In the processing range used, the density of specimens tended to decrease with increasing VED. This stands in stark contrast to other reports of increased density with increasing laser energy density [26,30,31]. The reason for this difference is that under a high VED, nickel, which has a lower melting point than titanium, volatilizes, resulting in an increase in holes and a decrease in density. Figures 2(b−d) show secondary electron images of the Ti−12Ni alloy printed at VEDs of 67, 133, and 267 J/mm^3, respectively, which are indicated by the purplish triangles in Fig. 2(a). It is evident that several roughly circular holes, whose diameter can reach about 50 μm, are present in the specimen produced at a VED of 267 J/mm^3.

3.2 Phase constitution

Figure 3 presents XRD patterns of LPBF-produced Ti−12Ni specimens at VEDs from 67 to 267 J/mm^3. The specimen produced at a VED of 67 J/mm^3 consisted of β-Ti, α-Ti, and Ti_2Ni phases, with the (110) diffraction peak of β-Ti exhibiting a great intensity. This suggests that a considerable quantity of β phase was retained at room temperature under the high cooling rate of LPBF. The other specimens consisted solely of the α-Ti and Ti_2Ni phases. The $(2\bar{1}\bar{1}0)$ diffraction peak of α-Ti exhibited the greatest intensity, indicating that the specimen matrix was α-Ti. As the VED increased, the diffraction peaks corresponding to α-Ti and Ti_2Ni increased in intensity. This is probably due to a reduction in dislocation density, which occurs when the powders are fully melted, resulting in a large grain size. Three specimens produced at VEDs of 67, 133, and 267 J/mm^3 were selected for further detailed investigations and denoted S1, S2, and S3, respectively.

3.3 Microstructural characteristics

In order to show the compositional segregation of the specimens under different VED conditions, the elemental distribution was analyzed using an electron probe microanalyzer (EPMA). As shown in Fig. 4, the elemental distribution became more homogeneous with increasing VED. Figure 5 shows the microstructure of Specimen S1. Obvious elemental segregation existed in the specimen, as shown in the backscattered electron (BSE) image in Fig. 5(a). Since the relative atomic mass of Ni is larger than that of Ti, the bright region indicated by blue arrows is Ni-rich, and the gray region indicated by yellow arrows is Ti-rich. Dendritic Ti_2Ni was distributed in the matrix, especially in the Ni-rich region. Figure 5(b) shows globular Ti_2Ni in more

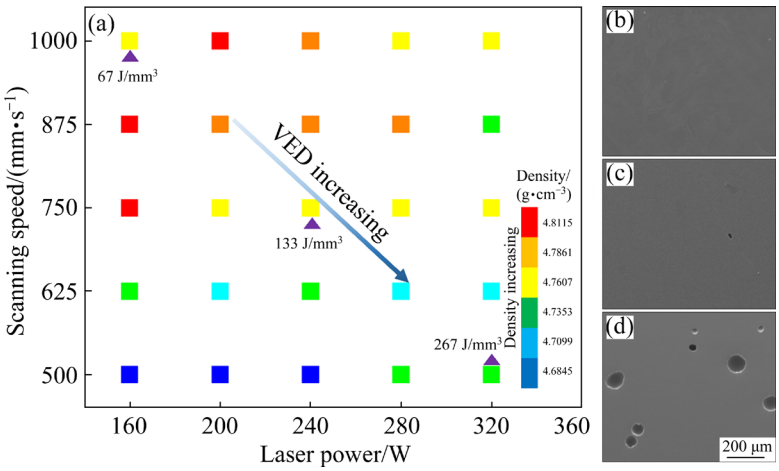

Fig. 2 (a) Density of LPBF-produced Ti−12Ni specimens under different processing parameters; (b−d) Secondary electron images of specimens produced at VEDs of 67, 133 and 267 J/mm^3, respectively

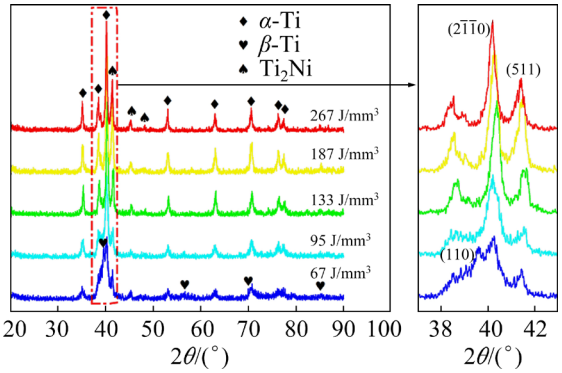

Fig. 3 XRD patterns of LPBF-produced Ti−12Ni specimens at different VEDs

detail. The EBSD results show that the β phase content is 93.9%, while the α phase and Ti_2Ni contents are 2% and 4.1%, respectively. This corresponds to the XRD results described above. The average grain size of the β phase was 20.4 μm.

The microstructure of Specimen S2 consisted of Ti_2Ni dendrites (indicated by blue arrows) interspersed in the matrix with globular Ti_2Ni (indicated by red arrows) dispersed in the inter-dendritic region, as shown in Figs. 6(a, b). The matrix was a lath eutectoid structure (indicated by the yellow arrows), exhibiting a feather-like distribution, as shown in Fig. 6(b). Compared with Specimen S1, there was less Ni segregation. The EBSD imaging results showed that the average grain size of the α phase was 0.5 μm. The β phase was completely transformed, and the α phase and Ti_2Ni contents were 75.2% and 24.5%, respectively.

TEM was used to further clarify details of the microstructure. As shown in Figs. 7(a, b), the pro-eutectoid Ti_2Ni precipitated mostly at the prior β phase grain boundaries with a small amount inside the β grains (indicated by purple arrows). The α laths (indicated by yellow arrows) were staggered with an average spacing of ~250 nm. The corresponding Ti and Ni EDS maps indicated the enriched Ni regions. Figure 7(c) shows the eutectoid structure. Globular Ti_2Ni (indicated by red arrows) was dispersed in the α laths, with an average size of ~150 nm. In addition, finer, short rod-like Ti_2Ni (indicated by blue arrows) with a radial size of about 50 nm was mostly located at the boundaries of the α laths. Figure 7(d) shows the pro-eutectoid Ti_2Ni in detail, and Fig. 7(e) shows a selected area electron diffraction (SAED) pattern from the red-circled region in Fig. 7(d). This

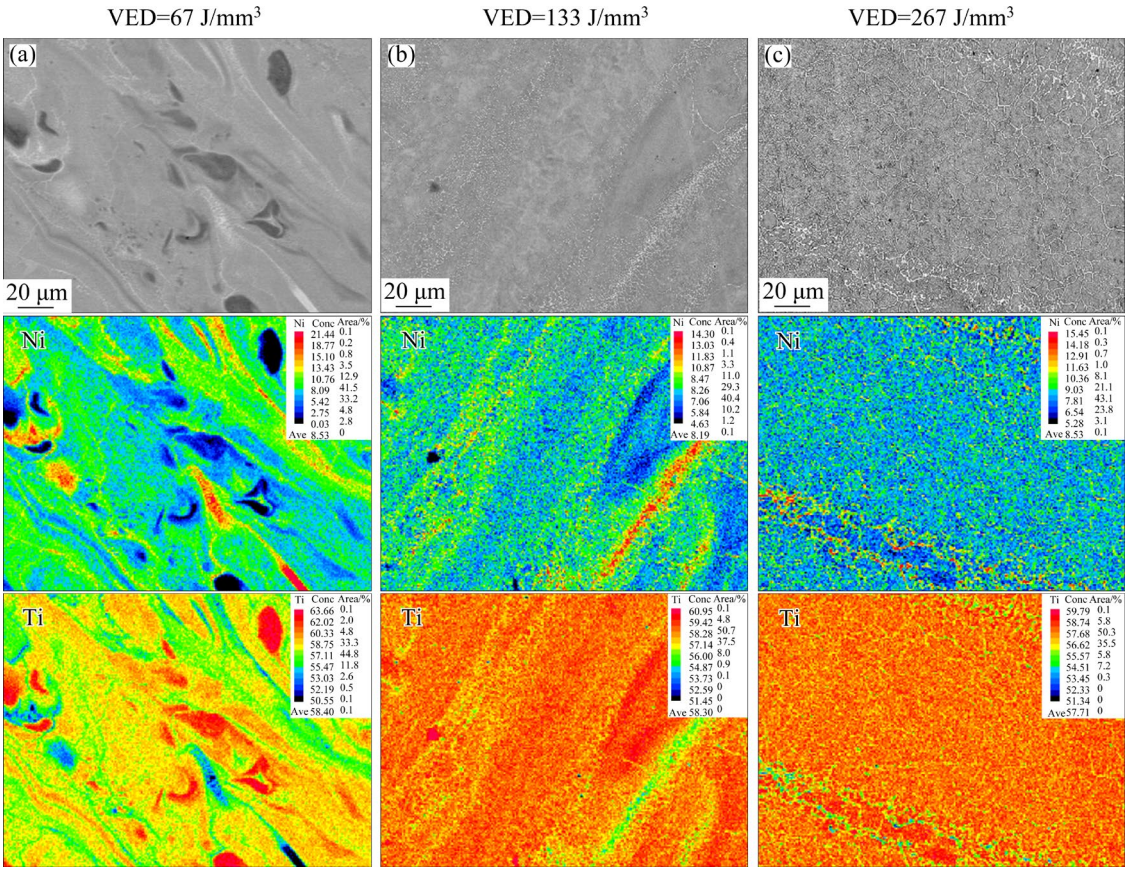

Fig. 4 EPMA elemental distribution maps of different specimens: (a) S1; (b) S2; (c) S3

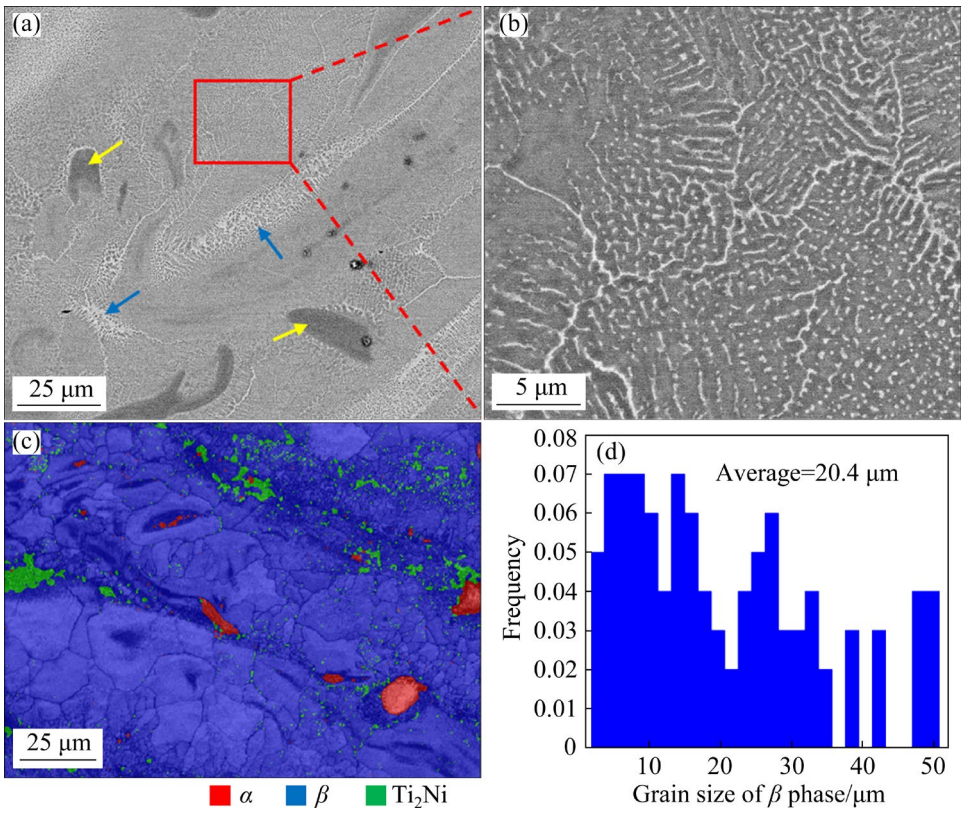

Fig. 5 BSE images (a, b), band contrast and phase map (c), and grain size distribution of β phase from EBSD results (d) for Specimen S1

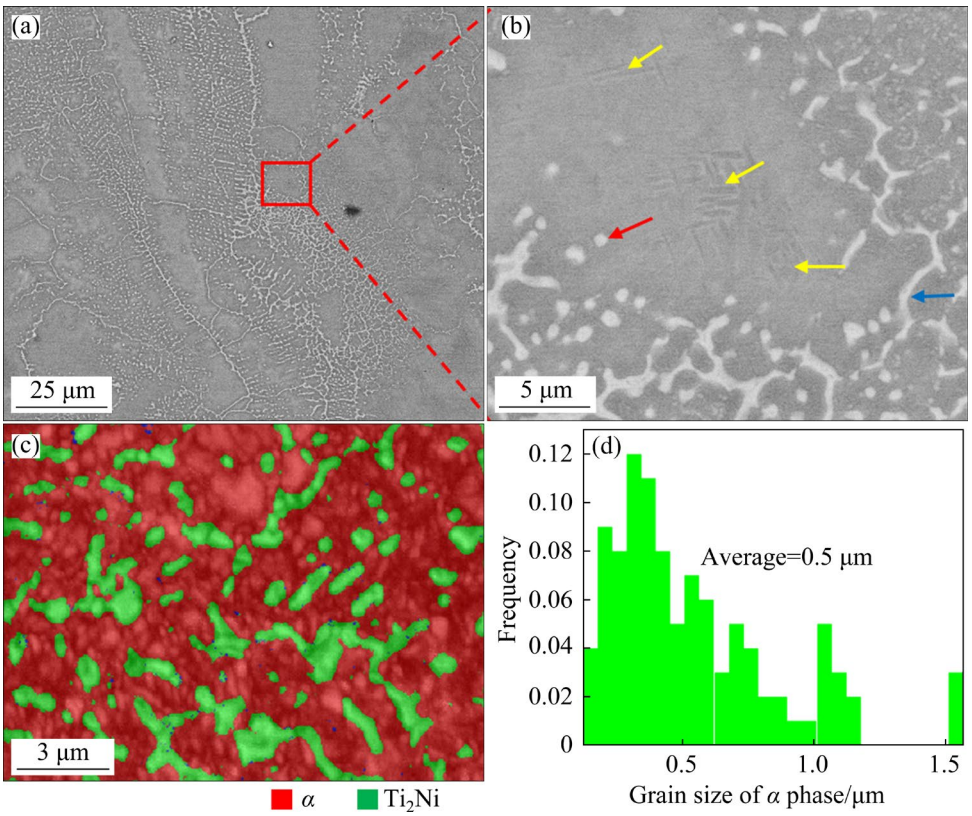

Fig. 6 BSE images (a, b), band contrast and phase map (c), and grain size distribution of α phase from EBSD results (d) for Specimen S2

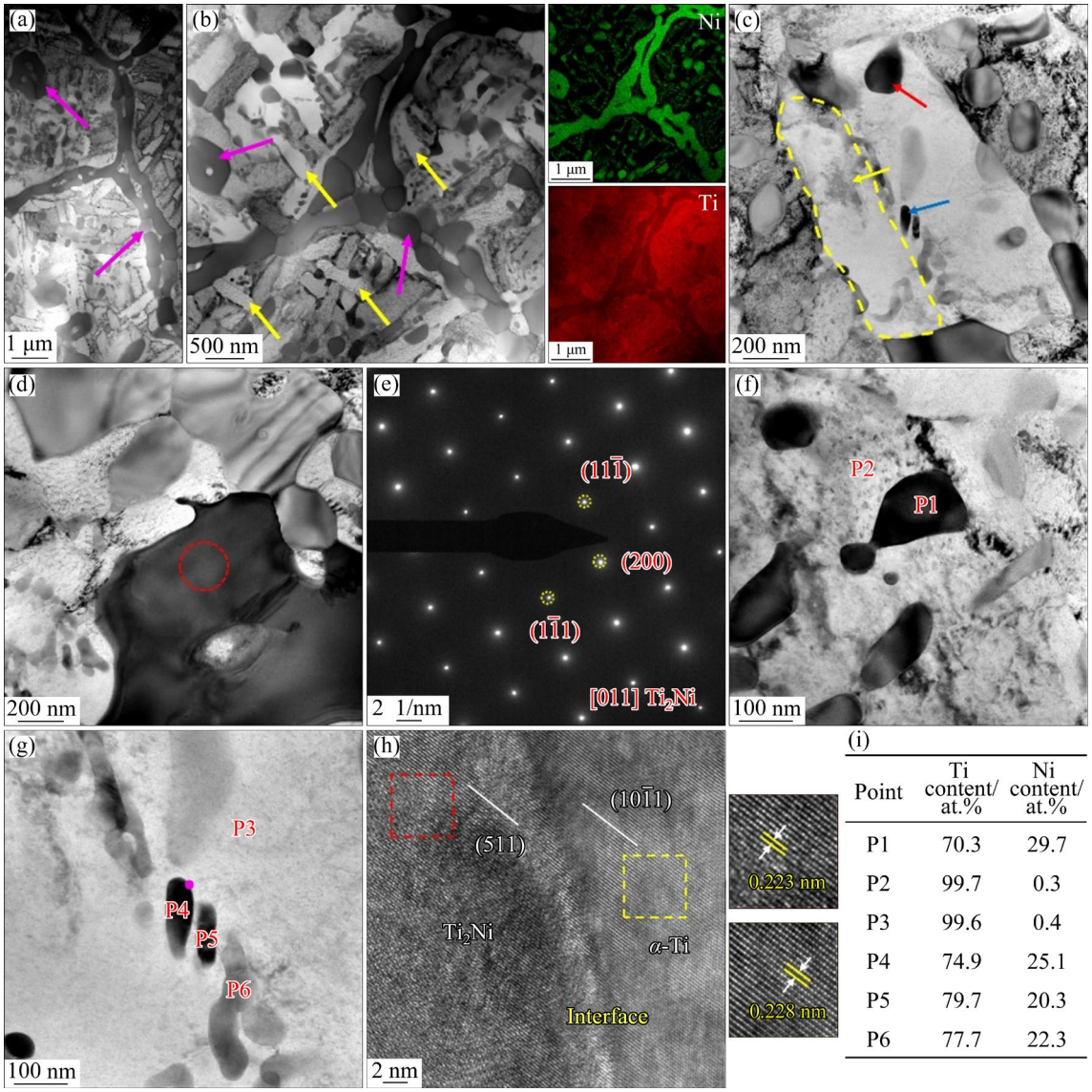

(i)

Point	Ti content/ at.%	Ni content/ at.%
P1	70.3	29.7
P2	99.7	0.3
P3	99.6	0.4
P4	74.9	25.1
P5	79.7	20.3
P6	77.7	22.3

Fig. 7 TEM analysis of Specimen S2: (a, b) BF images showing overall morphologies and corresponding EDS maps of Ti and Ni; (c) BF image showing eutectoid structure; (d) High-magnification BF image showing pro-eutectoid Ti_2Ni; (e) SAED pattern of red-circled region in (d); (f, g, i) High-magnification BF images of two types of Ti_2Ni precipitates and EDS point analysis results; (h) HRTEM image from purple dot in (g)

matches that of the intermetallic compound Ti_2Ni viewed along [011]. The compositional analysis results of the two types of eutectoid Ti_2Ni shown in Figs. 7(f, g) are summarized in Fig. 7(i). The results show that there was little Ni in the α matrix (P2 and P3). Both types of precipitate deviated from the stoichiometric Ti_2Ni composition and appeared to be Ti-rich. Compared with the globular precipitates (P1), the short rod-like precipitates (P4, P5, and P6) had a higher titanium content. The atomic-scale HRTEM image at the interface between short rod-like Ti_2Ni and the matrix α-Ti is depicted in Fig. 7(h). Enlarged views of the area enclosed by the red and yellow boxes are placed on the right. By measuring the distance between the crystal faces, the (511) plane of the Ti_2Ni and the $(10\bar{1}1)$ plane of the α-Ti can be distinguished.

Figures 8(a, b) show the microstructure of Specimen S3. This had a network of pro-eutectoid Ti_2Ni (indicated by blue arrows) along the prior β phase grain boundaries. In addition, globular Ti_2Ni particles were also present inside the primary β phase, as indicated by the red arrow. Several fine α phase laths were staggered within the region delineated by pro-eutectoid Ti_2Ni, as indicated by the yellow arrows. This is the result of the eutectoid

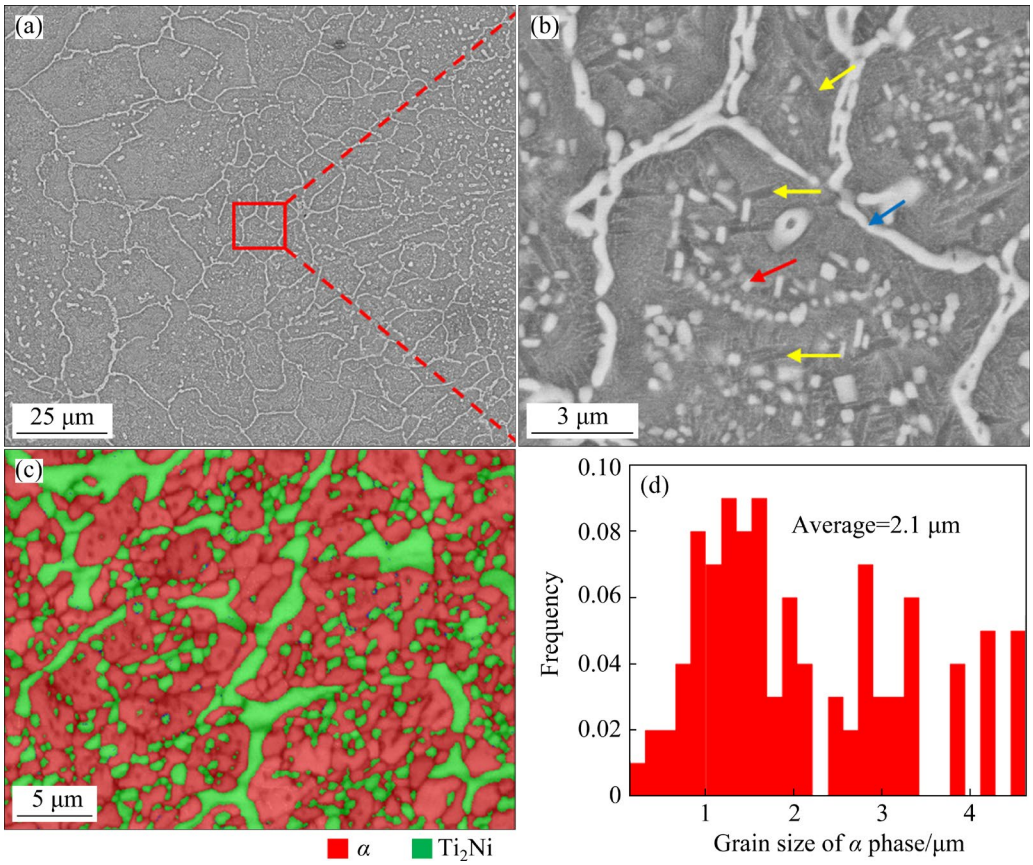

Fig. 8 BSE images (a, b), band contrast and phase map (c), and grain size distribution of α phase from EBSD results (d) for Specimen S3

transformation $\beta \rightarrow \alpha + Ti_2Ni$. Figures 8(c, d) show EBSD results. The phase maps further clarify the distribution of the phases, which is consistent with that depicted by the BSE images. The α phase and Ti_2Ni contents were 69.2% and 30.5% respectively. The average grain size of the α phase was 2.1 μm.

3.4 Mechanical properties

As noted earlier, the Ti−12Ni alloy produced by LPBF suffers from elemental segregation, especially at lower VEDs, which may impact its mechanical properties. Nanoindentation tests were performed on the matrix and Ni-rich regions of Specimens S1, S2, and S3. Figure 9(a) shows a representative set of nanoindentation load−displacement curves, and Figs. 9(b, c) show images of the nanoindentation locations for the matrix and Ni-rich regions. The nanohardness is inversely related to the depth of the indentation. The nanohardness (H) and elastic modulus (E) obtained from the nanoindentation test are presented in Figs. 9(d, e). Specimen S2 had the highest matrix nanohardness value among the three specimens, followed by Specimen S3. The nanohardness values of the S1, S2 and S3 substrates were (3.2±0.5), (7.8±0.1), and (3.7±0.5) GPa, respectively. The nanohardness of the Ni-rich region of Specimen S1 was (6.7±0.4) GPa, which was much higher than that of the matrix. In contrast, the Ni-rich region in Specimen S2 had a nanohardness of (5.4±0.3) GPa, which was lower than that of the matrix. The Ni-rich region in Specimen S3 had a nanohardness of (3.6±0.1) GPa, which was quite close to that of the matrix. The elastic modulus corresponding to each point was consistent with the nanohardness value. Higher hardness materials typically exhibited large elastic moduli, which indicated they were difficult to deform under steady strain.

To assess the impact of the VED on the mechanical properties of the printed Ti−12Ni alloy, compression tests were performed. The results are shown in Fig. 10. Except for the results between 88 and 100 J/mm^3, the alloy's compression properties show a trend of improving and then worsening with increasing VED. The maximum fracture strength of (1777±27) MPa was obtained at a VED of 133 J/mm^3

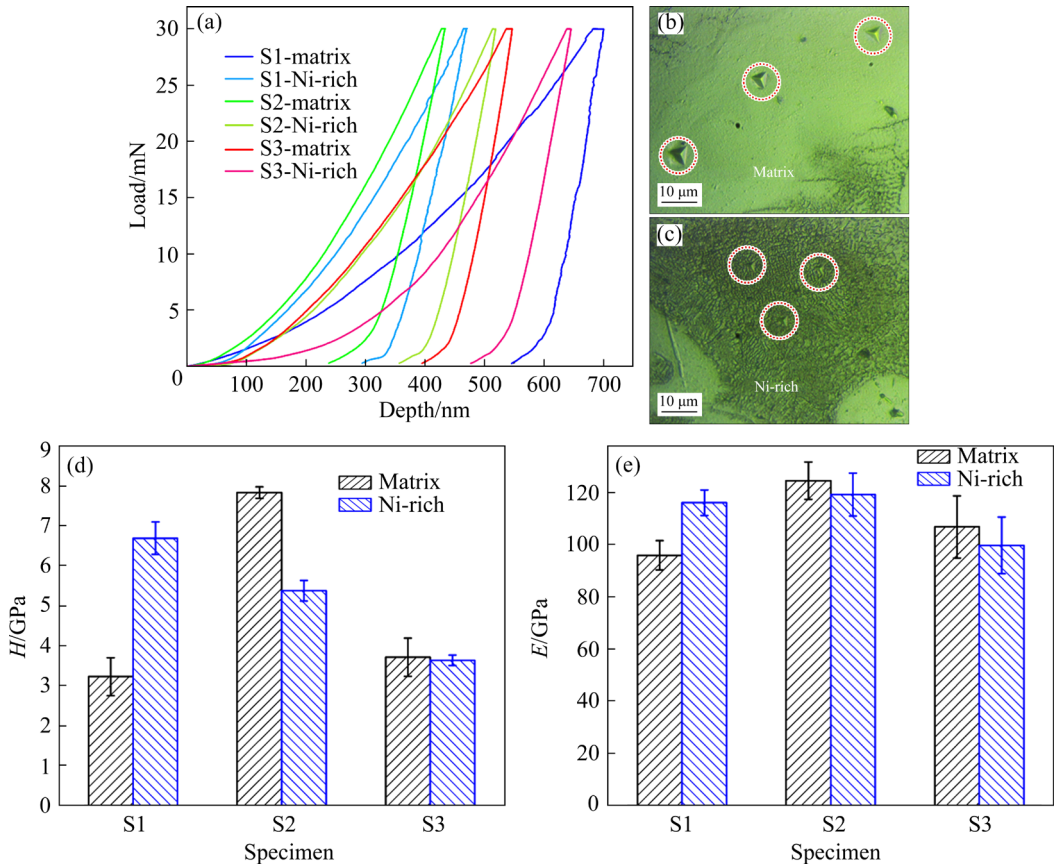

Fig. 9 (a) Nanoindentation load−displacement curves; (b, c) Nanoindentation positions of different microstructures in Specimen S1; (d, e) *H* and *E* values of different microstructures in different specimens, respectively

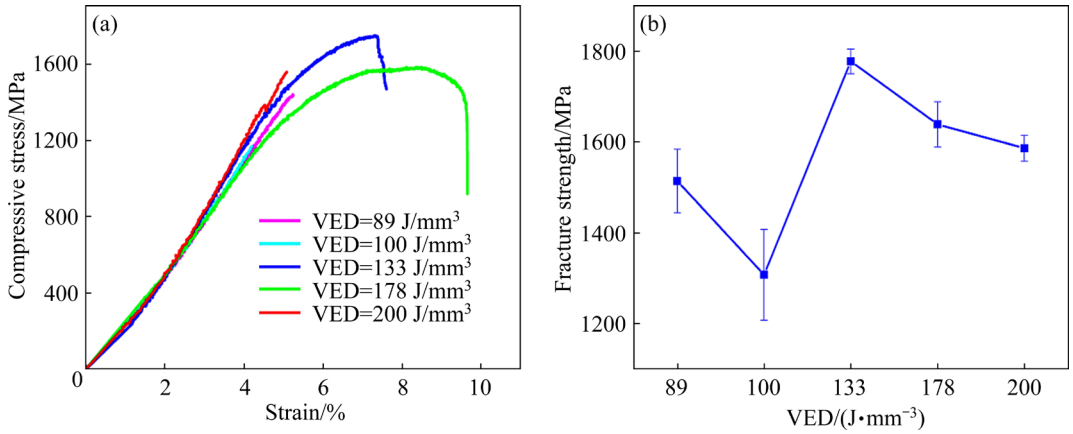

Fig. 10 Compressive true stress−strain curves (a) and fracture strengths (b) of LPBF-produced Ti−12Ni specimens at various VEDs

(Specimen S2). Notably, the specimens produced at VEDs of 133 and 178 J/mm^3 showed clear yielding and work hardening. All other specimens showed fractures before any plastic flow.

3.5 Potentiodynamic polarization characteristics

The potentiodynamic polarization curves of the Ti−12Ni specimens fabricated by LPBF in 3.5 wt.% NaCl solution under various VEDs are shown in Fig. 11. All specimens show typical polarization curves. As the potential increased in the first stage following anodic polarization, the current density rose. The second stage involved the formation of a protective passive layer on the surface of the specimens, which demonstrated stable passive behavior. The passive layer was

progressively dissolved in the third stage due to the high potential, and the fresh surface of the specimens was exposed to the solution again. Thus, the current density (J) continued to increase. Tafel slope extrapolation was used to calculate the corrosion potential (φ_{corr}) and corrosion current density (J_{corr}) from the polarization curves, as shown in Table 1. The results show that the corrosion potentials of Specimens S1, S2, and S3 were (−0.25±0.05), (−0.29±0.06), and (−0.30±0.02) V, respectively, and the corrosion current densities were (4.55±1.3), (48.39±9.7), and (17.54±2.4) nA/cm^2, respectively.

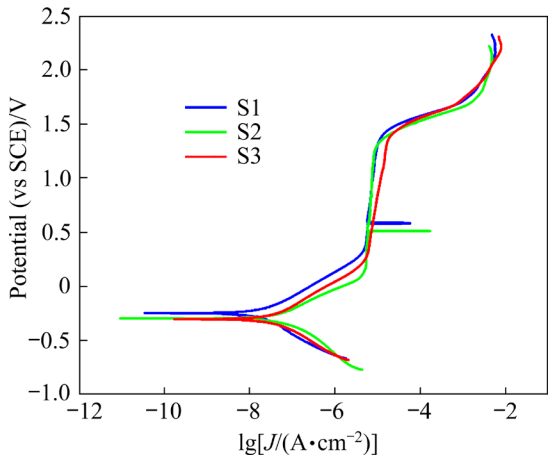

Fig. 11 Potentiodynamic polarization curves of LPBF-produced Ti−12Ni specimens in 3.5 wt.% NaCl solution

Table 1 Corrosion parameters obtained from potentiodynamic polarization curves

Specimen	φ_{corr} (vs SCE)/V	J_{corr}/(nA·cm^{-2})
S1	−0.25±0.05	4.55±1.3
S2	−0.29±0.06	48.39±9.7
S3	−0.30±0.02	17.54±2.4

The lowest corrosion current density occurred for Specimen S1, indicating that it had the best corrosion resistance [32]. Figure 12 presents the surface morphologies and corresponding EDS maps of the LPBF-produced Ti−12Ni under different VEDs after potentiodynamic polarization. Obvious corrosion traces were found in all specimens. Deep and wide pits appeared on the surface of Specimens S1 and S2, which were obvious corrosion pits. As can be seen from the EDS maps, pitting corrosion mainly occurred in the Ni-rich regions. However, the corrosion of Specimen S3 occurred in the holes formed during the LPBF processing.

4 Discussion

4.1 Microstructural evolution

Generally speaking, the quality of the formed part during LPBF processing depends on whether the laser is powerful enough to melt the powder [33]. A liquid molten pool will be produced when the powder is melted by the laser beam. In the molten pool, a surface tension gradient known as the Marango mudflow is caused by a temperature gradient produced by fast solidification [11]. A suitable VED increases the molten pool while also speeding up the diffusion of Ni and Ti due to the convection in the solution. Ni is not well suited for high VED printing [26,34]. Under the tremendous pressure of metal vaporization, the molten pool collapses, and pores are trapped at the bottom [31]. Although a high VED can prevent elemental segregation, it can cause pores to develop [35]. Thus, the trade-off between adjusting the VED to achieve adequate bonding and preventing molding defects must be considered.

Based on the observed microstructures under different VED conditions, it appears that the eutectoid-forming element Ni can refine the microstructure of LPBF-produced titanium alloys, which is also in line with the results reported in the literature [18−20]. Surprisingly, the microstructure of the Ti−12Ni alloy produced at a low VED (67 J/mm^3) shows a significant difference compared to that of specimens at higher VED, as evidenced by its retention of the vast majority of the β phase at room temperature. It is well known that the microstructural evolution behavior during continuous cooling is controlled by the cooling rate [36]. The observed microstructures under different VEDs can be rationalized according to the Ti−Ni binary phase diagram (Fig. 13(a)) and a schematic of the continuous cooling transformation (CCT) (Fig. 13(b)). During LPBF processing, the cooling rate decreases as the VED increases. Specimens S1, S2, and S3 correspond to cooling rates of v_1, v_2, and v_3, respectively, in Fig. 13(b), where $v_1>v_2>v_3$. Specimen S1 with a low VED possesses an ultra-high cooling rate corresponding to v_1 such that it does not intersect with the nose of the CCT diagram. In addition, Ni is a strong β-stabilizing element, which is capable of significantly lowering

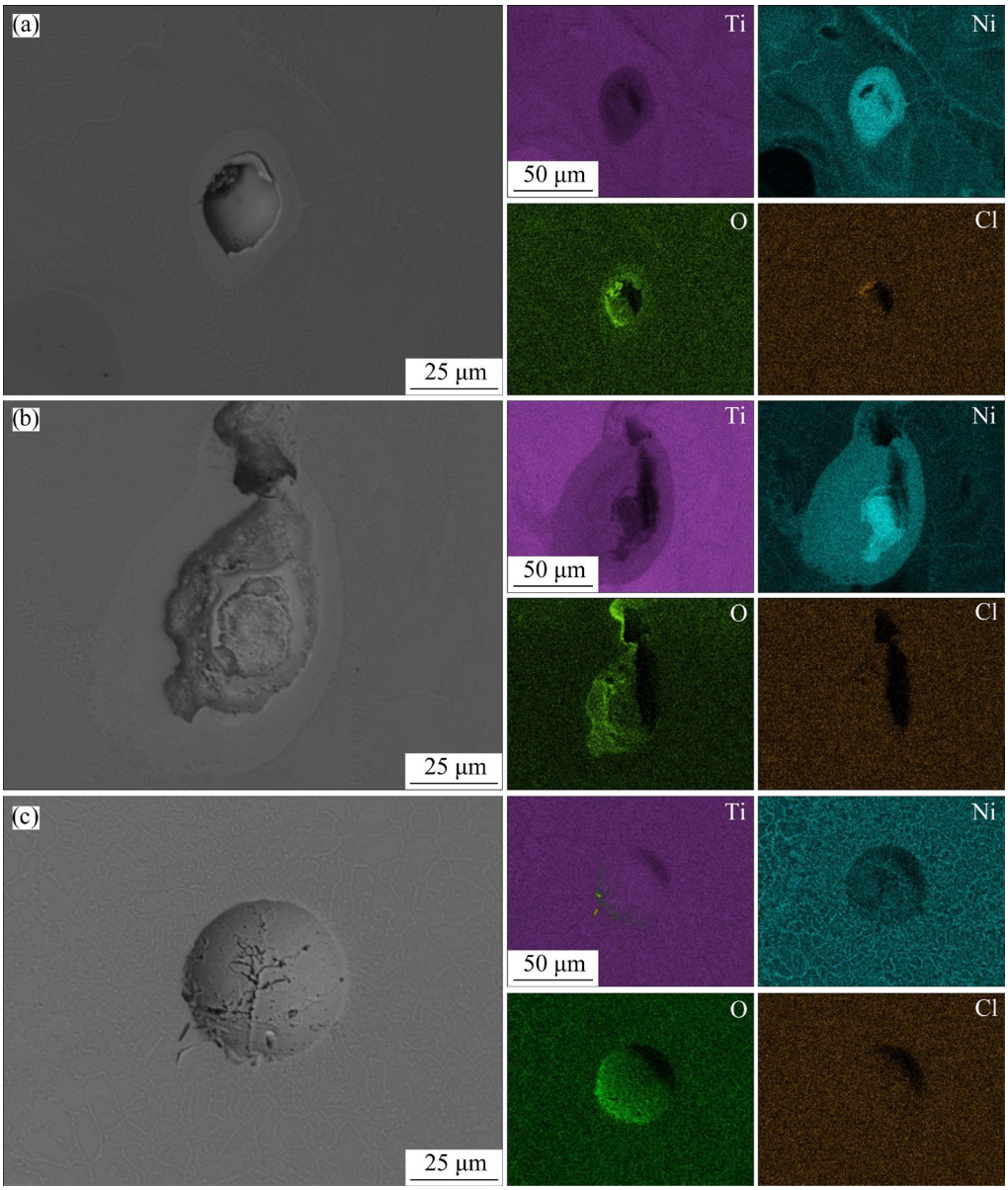

Fig. 12 BSE images showing surface morphologies after polarization testing and corresponding EDS maps of LPBF-produced Ti−12Ni specimens: (a) S1; (b) S2; (c) S3

the temperature of the $\beta \rightarrow \alpha + Ti_2Ni$ transformation [18]. Therefore, the β phase is retained too long for the transformation to occur.

The submicron eutectoid structure of Specimen S2 is expected. Elements such as Ni, Cu, Fe, Si, and B are used to refine the structure of additively-manufactured titanium alloys because of their high growth limiting factor Q values [16,17,37]. The high Q value indicates that Ni possesses the potential to refine the prior β grains. Because Ni diffuses rapidly in titanium, the eutectoid reaction occurs at the high cooling rate of the LPBF processing. During continuous cooling, Specimen S2 first undergoes the pro-eutectoid transformation of $\beta \rightarrow \beta + Ti_2Ni$, followed by the rapid eutectoid transformation of $\beta \rightarrow \alpha + Ti_2Ni$, as represented by v_2 in Fig. 13(b) [38,39]. The pro-eutectoid Ti_2Ni is mostly generated from the parent β grain boundaries, and retains the morphology of the prior β phases [40]. Some globular pro-eutectoid Ti_2Ni is also deposited within the β grains. The eutectoid microstructure consists of α laths and fine Ti_2Ni, which fill the remaining space in the β grains, as shown in Figs. 7(a, b). Figure 13(c) illustrates the typical phase transformation process. It has been reported that the eutectoid structure of Ti−Ni alloys prepared by casting and powder metallurgy exhibits a mixture

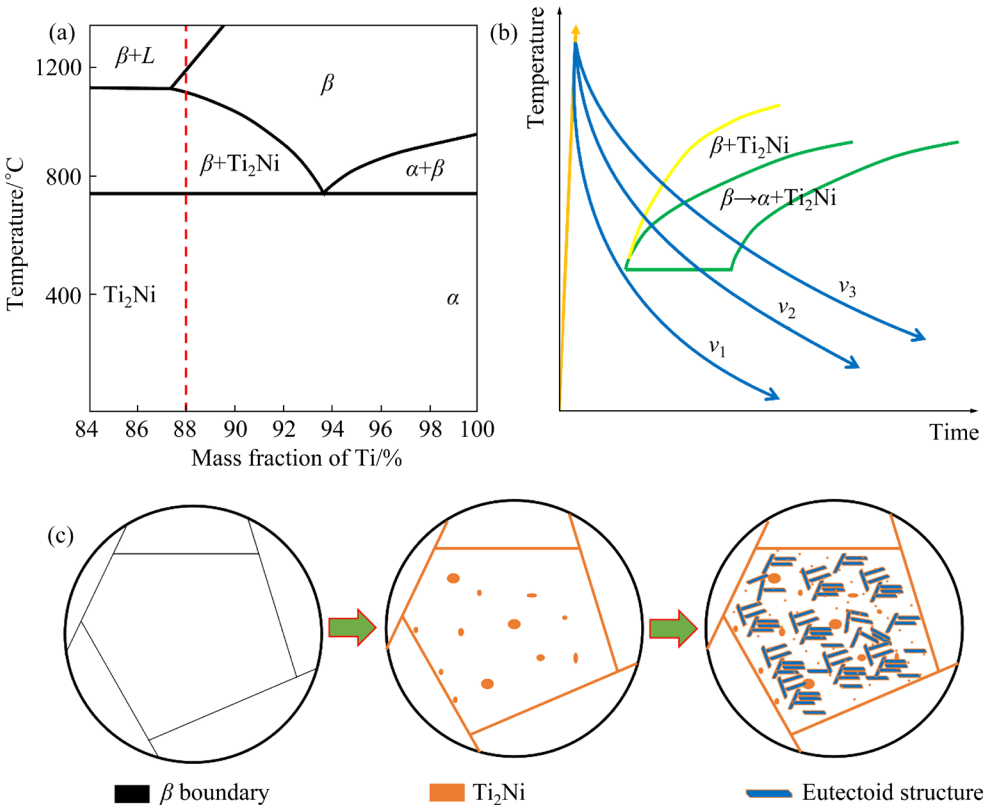

Fig. 13 (a) Part of Ti−Ni phase diagram indicating composition (12 wt.% Ni) selected for laser powder bed fusion; (b) Schematic of continuous cooling transformation (CCT) based on microstructures under different VEDs; (c) Schematic of microstructural evolution at cooling rates of v_2 and v_3

of lamellar α-Ti and Ti_2Ni [23]. However, Ti_2Ni generated by the eutectoid reaction in Specimen S2 exhibits a nonlamellar nature. In addition, it is clear from the TEM−EDS results that the Ni content of the precipitated phase was significantly lower than 33 at.%, especially in the short rod-shaped precipitates (Fig. 7(g)) located at the α lath boundaries. These observations suggest that under the high cooling rates of LPBF processing, short-range diffusion still takes place, allowing Ni to separate from the titanium matrix to form Ti_2Ni. As a result, the composition of Ti_2Ni deviates from its equilibrium condition. Subsequently, the cyclic heat treatment and even remelting process cause the short rod-like Ti_2Ni to grow and spheroidize, thus forming globular Ti_2Ni (Fig. 7(f)) in α laths. As a result of adequate diffusion, the Ni content in globular Ti_2Ni is more closely aligned with the equilibrium state.

The phase transformation path experienced by Specimen S3 is shown as v_3 in Fig. 13(b). It is similar to Specimen S2. The pro-eutectoid product Ti_2Ni decorates the prior β grain boundaries and connects with each other in a network. At high VEDs, it has the most time to undergo various reactions and for elemental partitioning to occur. In addition, its in-situ heat treatment produces a larger heat affected zone and higher temperatures. The eutectoid structure has longer time to grow. Thus, its eutectoid microstructure is clearly seen in BSE images [41]. However, the slower cooling rate leads to an increase in the average grain size compared to Specimen S2.

4.2 Mechanical properties

As mentioned above, the morphologies of LPBF-produced Ti−12Ni alloys under different VEDs are significantly different. The microstructures of specimens prepared at the same VED are also different due to elemental segregation. Nanoindentation test can be used to measure micromechanical behavior. Differences in nanohardness are caused by different microstructures. In titanium alloys, the hardness of the α phase is greater than that of the β phase due to different crystal structures [42]. Thus, the lowest

nanohardness was found for the matrix in Specimen S1. However, the nanohardness of Specimen S2 was higher than that of Specimen S3, which was due to the coarsening of the microstructure under the action of the high VED in Specimen S3. For Specimen S1, the matrix consisted of coarse β phase grains, while the Ni-rich regions had fine grains reinforced by Ti_2Ni, as shown in Fig. 5(c). As a result, the Ni-rich region had a higher nanohardness than the matrix. In contrast, in Specimen S2, the matrix was a fine eutectoid structure with nano-sized Ti-rich Ti_2Ni grains diffusely distributed in the α laths. When subjected to indentation loading, dislocation nucleation and strain transfer occur near the grain boundaries, and the dispersed particles tend to resist the dislocation motion exerted by the indentation, thus producing a high hardness and a high elastic modulus [43]. The deformation between the coarse Ti_2Ni and the matrix in the Ni-rich regions was not synchronized. The resulting stress concentrations led to premature cracking, thus resulting in a lower nanohardness [23]. It can be seen that although Ti_2Ni, as a hard intermediate phase, can strengthen titanium alloys, its morphology and distribution have a crucial impact.

The compressive properties of LPBF-produced Ti−12Ni alloy are mainly related to the following two features. On the one hand, with increasing the VED, elemental segregation decreases. The coarse Ti_2Ni formed at Ni segregation is susceptible to generating stress concentrations at the interface with the matrix during the compression process. The initiation and rapid propagation of cracks lead to the premature failure of the specimen. In addition, the weak links caused by insufficient bonding are greatly reduced, thus the force transfer and deformation are enhanced [44]. However, the porosity formed by a high VED can be a fatal flaw during mechanical testing. Specimen S2 prepared under a medium VED possesses a balanced forming quality. On the other hand, the strength of polycrystals (σ_m) increases with grain refinement [45]. The Hall−Petch relationship is as follows [46]:

$$\sigma_m=\sigma_0+k_m d^{-1/2} \quad (2)$$

where σ_0 is the lattice resistance, k_m represents the grain boundary resistance to slip transfer, and d is the grain size. As mentioned above, Specimen S2 has small grain size and dispersed nanoscale Ti_2Ni. During the compressive deformation process, dislocations are formed within the α grains and held in place by grain boundaries and diffused Ti_2Ni, thus improving the strength [28,47]. Furthermore, the nanoscale Ti_2Ni can effectively alleviate stress concentration, allowing the plastic flow to proceed [22]. As the stress is further intensified, microcracks are formed gradually. The dispersion of nano-Ti_2Ni results in the deflection of microcrack propagation, thereby delaying the failure of the specimen [48]. Combining these effects, it is not surprising that Specimen S2 possesses the best compressive performance.

4.3 Corrosion properties

The corrosion properties of titanium alloys are determined by the phases present and the microstructure. The segregation of Ni promotes the local growth in the β phase. Different volume fractions of the β phase result in different electrochemical activity [49]. As the oxide film that forms on the β phase is more stable than that on the α phase, it has been demonstrated that the β phase plays a significant role in enhancing the corrosion resistance of titanium alloys [50]. Specimen S1 possesses the best corrosion resistance since it has a β phase content of up to 93.9%. The passive coating on the surface of titanium alloys is attacked by Cl^-, leading to pitting corrosion [51]. Because titanium has a greater $-\Delta G$ value than nickel, when Ti−Ni alloys are corroded, nickel tends to form $Ni(OH)_2$ and titanium tends to form dense TiO_2. In addition, the Ti_2Ni phase is a high-energy zone with a more negative electric potential relative to the titanium matrix. This heterogeneous structure has been proven to be preferentially corroded [32,52]. The corrosion mechanism can be explained as the establishment of a corrosion microcell on the electrode surface between the Ti_2Ni and the titanium matrix. Therefore, significant corrosion occurs in the Ni-rich regions. This is consistent with the EDS maps (Figs. 12(a, b)) of the specimen surface after corrosion. Furthermore, at a potential of ~0.6 V, two small plateaus occur on the polarization curves of Specimens S1 and S2, where the current density increases rapidly, indicating the occurrence of pitting corrosion. The distribution of titanium and nickel is also an important factor affecting the stability of the passive film [11,32]. A uniform distribution avoids electrical interaction

and facilitates a high quality TiO_2 oxide film on the surface of the specimen, thus, producing better corrosion resistance. Specimen S3 had the most homogeneous elemental distribution and therefore produced a passive film with better corrosion resistance than Specimen S2, which had similar phases present. However, it had more holes, and the corrosion mainly occurred in the holes.

5 Conclusions

(1) As the VED was increased from 67 to 267 J/mm^3, greater porosity occurred, which led to a decrease in the density, but the segregation of Ni elements was reduced. At a low VED (Specimen S1), a titanium alloy with a nearly β-phase structure was produced. At higher VEDs (Specimens S2 and S3), the microstructures were mostly pro-eutectoid Ti_2Ni and a fine eutectoid structure (α+Ti_2Ni).

(2) Specimen S2 (133 J/mm^3) matrix exhibited the highest nanohardness and elastic modulus, which indicated that small, dispersed Ti_2Ni particles in the eutectoid structure strengthened titanium alloys more greatly than coarse pro-eutectoid Ti_2Ni. Specimen S2 showed the best compressive properties with a fracture strength of (1777±27) MPa, due to its easy-forming quality, fine grains and the strengthening effect of nanoscale Ti_2Ni.

(3) Specimen S1 with a near β-phase structure had the best corrosion resistance, with a corrosion potential of (−0.25±0.05) V and a corrosion current density of (4.55±1.3) nA/cm^2, respectively. Specimens S1 and S2 showed corrosion pitting in their Ni-rich regions, whereas corrosion in Specimen S3 occurred mainly in the holes formed during processing.

CRediT authorship contribution statement

Kai HUANG: Conceptualization, Data curation, Methodology, Writing − Original draft; **Yao-jia REN:** Conceptualization, Formal analysis, Investigation, Methodology; **Qing-ge WANG:** Conceptualization, Formal analysis, Writing − Review & editing; **Yi LIU:** Conceptualization, Formal analysis, Methodology, Resources; **Quan FU:** Conceptualization, Formal analysis; **Ning LI:** Conceptualization, Writing − Review & editing; **Ian BAKER:** Conceptualization, Writing − Review & editing; **Min SONG:** Conceptualization, Formal analysis; **Hong WU:** Funding acquisition, Supervision, Project administration, Writing − Review & editing.

Declaration of competing interest

The authors declare that they have no known competing financial interests or personal relationships that could have appeared to influence the work reported in this paper.

Acknowledgments

This research was supported by the National Natural Science Foundation of China (Nos. 12374022, U23A20540), the Technological Base Project, China (No. JSHS2022206A001), the Natural Science Foundation of Hunan Province for Distinguished Young Scholars, China (No. 2023JJ10075), the Scientific and Technological Project of Yunnan Precious Metals Laboratory, China (No. YPML-202305247), and the Central South University Research Program of Advanced Interdisciplinary Studies, China (No. 2023QYJC038). Authors would also like to thank Sinoma Institute of Materials Research (Guang Zhou) Co., Ltd., for assistance with TEM characterization and the Electron Microscope Center of KAIPLE Co., Ltd., (Changsha, China) for the support of EBSD characterization. Ian BAKER was supported by Dartmouth College, USA.

References

[1] ZHU Yu-man, ZHANG Kun, MENG Zhi-chao, ZHANG Kai, HODGSON P, BIRBILIS N, WEYLAND M, FRASER H L, LIM S C V, PENG Hui-zhi, YANG Rui, WANG Hao, HUANG Ai-jun. Ultrastrong nanotwinned titanium alloys through additive manufacturing [J]. Nature Materials, 2022, 21(11): 1258−1262.

[2] WU Yong, FAN Rong-lei, QIN Zhong-huan, CHEN Ming-he. Shape controlling and property optimization of TA32 titanium alloy thin-walled part prepared by hot forming [J]. Transactions of Nonferrous Metals Society of China, 2021, 31(8): 2336−2357.

[3] XIAO Yi, LANG Li-hui, XU Wen-cai, ZHANG De-xin. Diffusion bonding of Ti−6Al−4V titanium alloy powder and solid by hot isostatic pressing [J]. Transactions of Nonferrous Metals Society of China, 2022, 32(11): 3587−3595.

[4] SCHAAL H, CASTANY P, GLORIANT T. Outstanding strain-hardening of a new metastable β-titanium alloy elaborated by in situ additive manufacturing L-PBF process [J]. Materials Science and Engineering: A, 2023, 875: 145117.

[5] ZHANG Lai-chang, ATTAR H. Selective laser melting of titanium alloys and titanium matrix composites for biomedical applications: A review [J]. Advanced Engineering Materials, 2016, 18(4): 463−475.

[6] WANG Di, YANG Yong-qiang, WANG Ying-jun, YANG Li, WANG Hao, YANG Shou-feng. Introduction to the special issue on design and simulation in additive manufacturing [J]. Computer Modeling in Engineering & Sciences, 2021, 126(1): 1−4.

[7] YU Ai-hua, XU Wei, LU Xin, TAMADDON M, LIU Bo-wen, TIAN Shi-wei, ZHANG Ce, MUGHAL M A, ZHANG Jia-zhen, LIU Chao-zong. Development and characterizations of graded porous titanium scaffolds via selective laser melting for orthopedics applications [J]. Transactions of Nonferrous Metals Society of China, 2023, 33(6): 1755−1767.

[8] FAN Hai-yang, LIU Ya-hui, YANG Shou-feng. Martensite decomposition during post-heat treatments and the aging response of near-α Ti−6Al−2Sn−4Zr−2Mo (Ti-6242) titanium alloy processed by selective laser melting (SLM) [J]. Journal of Micromechanics and Molecular Physics, 2021, 6(2): 2050018.

[9] SUI Shang, CHEW You-xiang, HAO Zhi-wei, WENG Fei, TAN Chao-lin, DU Zheng-lin, BI Gui-jun. Effect of cyclic heat treatment on microstructure and mechanical properties of laser aided additive manufacturing Ti−6Al−2Sn−4Zr−2Mo alloy [J]. Advanced Powder Materials, 2022, 1(1): 100002.

[10] ZHANG Tian-long, LIU C T. Design of titanium alloys by additive manufacturing: A critical review [J]. Advanced Powder Materials, 2022, 1(1): 100014.

[11] ZHAO Dan-lei, HAN Chang-jun, LI Yan, LI Jing-jing, ZHOU Kun, WEI Qing-song, LIU Jie, SHI Yu-sheng. Improvement on mechanical properties and corrosion resistance of titanium−tantalum alloys in-situ fabricated via selective laser melting [J]. Journal of Alloys and Compounds, 2019, 804: 288−298.

[12] BERMINGHAM M J, STJOHN D H, KRYNEN J, TEDMAN J S, DARGUSCH M S. Promoting the columnar to equiaxed transition and grain refinement of titanium alloys during additive manufacturing [J]. Acta Materialia, 2019, 168: 261−274.

[13] LIU Yan-jun, XU Long-bin, QIU Chun-lei. Development of an additively manufactured metastable beta titanium alloy with a fully equiaxed grain structure and ultrahigh yield strength [J]. Additive Manufacturing, 2022, 60: 103208.

[14] NG C H, BERMINGHAM M J, DARGUSCH M S. Controlling grain size, morphology and texture in additively manufactured β-titanium alloy with super transus hot isostatic pressing [J]. Additive Manufacturing, 2022, 59: 103176.

[15] CHEN Yuan-hang, YANG Chun-li, FAN Cheng-lei, ZHUO Yi-min, LIN San-bao, CHEN Chao. Grain refinement of additive manufactured Ti−6.5Al−3.5Mo−1.5Zr−0.3Si titanium alloy by the addition of La_2O_3 [J]. Materials Letters, 2020, 275: 128170.

[16] ZHANG D Y, QIU D, GIBSON M A, ZHENG Y F, FRASER H L, STJOHN D H, EASTON M A. Additive manufacturing of ultrafine-grained high-strength titanium alloys [J]. Nature, 2019, 576: 91−95.

[17] BERMINGHAM M J, MCDONALD S D, STJOHN D H, DARGUSCH M S. Beryllium as a grain refiner in titanium alloys [J]. Journal of Alloys and Compounds, 2009, 481(1/2): L20−L23.

[18] XIONG Zhi-hui, PANG Xiao-tong, LIU Shi-long, LI Zhu-guo, MISRA R D K. Hierarchical refinement of nickel-microalloyed titanium during additive manufacturing [J]. Scripta Materialia, 2021, 195: 113727.

[19] XUE Ai-tang, LIN Xin, WANG Li-lin, LU Xu-fei, YUAN Lu-kai, DING Han-lin, HUANG Wei-dong. Achieving fully-equiaxed fine β-grains in titanium alloy produced by additive manufacturing [J]. Materials Research Letters, 2023, 11(1): 60−68.

[20] NARAYANA P L, KIM J H, LEE S W, WON J W, PARK C H, YEOM J T, REDDY N S, HONG J K. Novel eutectoid Ti−5Ni alloy fabricated via direct energy deposition [J]. Scripta Materialia, 2021, 200: 113918.

[21] LI S, HASSANIN H, ATTALLAH M M, ADKINS N J E, ESSA K. The development of TiNi-based negative Poisson's ratio structure using selective laser melting [J]. Acta Materialia, 2016, 105: 75−83.

[22] LU H Z, LIU L S, YANG C, LUO X, SONG C H, WANG Z M, WANG J, SU Y D, DING Y F, ZHANG L C, LI Y Y. Simultaneous enhancement of mechanical and shape memory properties by heat-treatment homogenization of Ti_2Ni precipitates in TiNi shape memory alloy fabricated by selective laser melting [J]. Journal of Materials Science & Technology, 2022, 101: 205−216.

[23] KIM J S, HONG S Y, PARK K, PARK J H, KIM J K. Casting microstructure and phase-specific deformation behavior of Ti−20Ni alloy containing Ti_2Ni phase [J]. Materials Today Communications, 2023, 36: 106549.

[24] CAO Liu. Mesoscopic-scale numerical investigation including the influence of process parameters on LPBF multi-layer multi-path formation [J]. Computer Modeling in Engineering & Sciences, 2021, 126(1): 5−23.

[25] SUN Jin-e, ZHANG Bai-cheng, QU Xuan-hui. High strength Al alloy development for laser powder bed fusion [J]. Journal of Micromechanics and Molecular Physics, 2021, 6(6): 2141001.

[26] STEGMAN B, SHANG A Y, HOPPENRATH L, RAJ A, ABDEL K H, SUTHERLAND J, SCHICK D, MORGAN V, JACKSON K, ZHANG X H. Volumetric energy density impact on mechanical properties of additively manufactured 718 Ni alloy [J]. Materials Science and Engineering: A, 2022, 854: 143699.

[27] WU Hong, REN Yao-jia, REN Jun-ye, LIANG Lu-xin, LI Rui-di, FANG Qi-hong, CAI An-hui, SHAN Quan, TIAN Ying-tao, BAKER I. Selective laser melted $AlSi_{10}Mg$ alloy under melting mode transition: Microstructure evolution, nanomechanical behaviors and tensile properties [J]. Journal of Alloys and Compounds, 2021, 873: 159823.

[28] LU Hai-zhou, YANG Chao, LUO Xuan, MA Hong-wei, SONG Bo, LI Yuan-yuan, ZHANG Lai-chang. Ultrahigh-performance TiNi shape memory alloy by 4D printing [J]. Materials Science and Engineering: A, 2019, 763: 138166.

[29] GU Dong-dong, MA Cheng-long. In-situ formation of Ni_4Ti_3 precipitate and its effect on pseudoelasticity in selective laser melting additive manufactured NiTi-based composites [J]. Applied Surface Science, 2018, 441: 862−870.

[30] KEMPEN K, THIJS L, van HUMBEECK J, KRUTH J P. Processing $AlSi_{10}Mg$ by selective laser melting: Parameter optimisation and material characterisation [J]. Materials Science and Technology, 2015, 31(8): 917−923.

[31] LEICHT A, RASHIDI M, KLEMENT U, HRYHA E. Effect of process parameters on the microstructure, tensile strength and productivity of 316L parts produced by laser powder bed

fusion [J]. Materials Characterization, 2020, 159: 110016.

[32] QIN Peng, LIU Yu-jing, SERCOMBE T B, LI Yu-hua, ZHANG Chuan-wei, CAO Chong-de, SUN Hong-qi, ZHANG Lai-chang. Improved corrosion resistance on selective laser melting produced Ti−5Cu alloy after heat treatment [J]. ACS Biomaterials Science & Engineering, 2018, 4(7): 2633−2642.

[33] SAEDI S, SHAYESTEH M N, AMERINATANZI A, ELAHINIA M, KARACA H E. On the effects of selective laser melting process parameters on microstructure and thermomechanical response of Ni-rich NiTi [J]. Acta Materialia, 2018, 144: 552−560.

[34] WATRING D S, BENZING J T, HRABE N, SPEAR A D. Effects of laser-energy density and build orientation on the structure−property relationships in as-built Inconel 718 manufactured by laser powder bed fusion [J]. Additive Manufacturing, 2020, 36: 101425.

[35] LIU Ming-yu, WANG Jiang, HU Tao, XU Song-zhe, SHUAI San-san, XUAN Wei-dong, YIN Shuo, CHEN Chao-yue, REN Zhong-ming. Laser powder bed fusion of a Ni_3Al-based intermetallic alloy with tailored microstructure and superior mechanical performance [J]. Advanced Powder Materials, 2024, 3(1): 100152.

[36] ZHAO Dong, CHEN Yong-nan, JIANG Chao-ping, LI Yao, ZHAO Qin-yang, XU Yi-ku, ZHAN Hai-fei, WAN Ming-pan, ZHAO Yong-qing. Morphological evolution of Ti_2Cu in Ti−13Cu−Al alloy after cooling from semi-solid state [J]. Journal of Alloys and Compounds, 2020, 848: 156639.

[37] LEE D H, SEOK M Y, ZHAO Y K, CHOI I C, HE J Y, LU Z P, SUH J Y, RAMAMURTY U, KAWASAKI M, LANGDON T G, JANG J. Spherical nanoindentation creep behavior of nanocrystalline and coarse-grained CoCrFeMnNi high-entropy alloys [J]. Acta Materialia, 2016, 109: 314−322.

[38] MING Hui, ZHU Cheng-peng, SONG Xue-yan, ZHANG Xiao-yong, ZHOU Ke-chao. Microstructure evolution and mechanical properties of Ti-1023 alloy during β slow cooling process [J]. Transactions of Nonferrous Metals Society of China, 2023, 33(12): 3685−3698.

[39] ZHANG Chang-jiang, JIANG Xi, LU Zhi-dan, FENG Hong, ZHANG Shu-zhi, XU Ying, HAYAT M D, CAO Peng. Effect of duplex aging on microstructure and mechanical properties of near-β titanium alloy processed by isothermal multidirectional forging [J]. Transactions of Nonferrous Metals Society of China, 2022, 32(4): 1159−1168.

[40] DONTHULA H, VISHWANADH B, ALAM T, BORKAR T, CONTIERI R J, CARAM R, BANERJEE R, TEWARI R, DEY G K, BANERJEE S. Morphological evolution of transformation products and eutectoid transformation(s) in a hyper-eutectoid Ti−12at.%Cu alloy [J]. Acta Materialia, 2019, 168: 63−75.

[41] MANTRI S A, ALAM T, ZHENG Y, WILLIAMS J C, BANERJEE R. Influence of post deposition annealing on microstructure and properties of laser additively manufactured titanium copper alloys [J]. Additive Manufacturing, 2020, 32: 101067.

[42] SABZI H E. Powder bed fusion additive layer manufacturing of titanium alloys [J]. Materials Science and Technology, 2019, 35(8): 875−890.

[43] ATTAR H, EHTEMAM H S, KENT D, OKULOV I V, WENDROCK H, BÖENISCH M, VOLEGOV A S, CALIN M, ECKERT J, DARGUSCH M S. Nanoindentation and wear properties of Ti and Ti−TiB composite materials produced by selective laser melting [J]. Materials Science and Engineering: A, 2017, 688: 20−26.

[44] REN Yao-jia, LIANG Lu-xin, SHAN Quan, CAI An-hui, DU Jing-guang, HUANG Qian-li, LIU Shi-feng, YANG Xin, TIAN Ying-tao, WU Hong. Effect of volumetric energy density on microstructure and tribological properties of FeCoNiCuAl high-entropy alloy produced by laser powder bed fusion [J]. Virtual and Physical Prototyping, 2020, 15(Suppl.): 543−554.

[45] KOTHARI K, RADHAKRISHNAN R, WERELEY N M. Advances in gamma titanium aluminides and their manufacturing techniques [J]. Progress in Aerospace Sciences, 2012, 55: 1−16.

[46] HUANG Dan-ni, TAN Qi-yang, ZHOU Ying-hao, YIN Yu, WANG Feng, WU Tao, YANG Xian-liang, FAN Zhi-qi, LIU Yin-gang, ZHANG Jing-qi, HUANG Han, YAN Ming, ZHANG Ming-xing. The significant impact of grain refiner on γ-TiAl intermetallic fabricated by laser-based additive manufacturing [J]. Additive Manufacturing, 2021, 46: 102172.

[47] LU Hai-zhou, MA Hong-wei, CAI Wei-si, LUO Xuan, WANG Zhi, SONG Chang-hui, YIN Shuo, YANG Chao. Stable tensile recovery strain induced by a Ni_4Ti_3 nanoprecipitate in a $Ni_{50.4}Ti_{49.6}$ shape memory alloy fabricated via selective laser melting [J]. Acta Materialia, 2021, 219: 117261.

[48] LIU Shi-feng, HAN Song, ZHANG Ling, CHEN Liang-yu, WANG Li-qiang, ZHANG Liang, TANG Yu-jin, LIU Jia, TANG Hui-ping, ZHANG Lai-chang. Strengthening mechanism and micropillar analysis of high-strength NiTi−Nb eutectic-type alloy prepared by laser powder bed fusion [J]. Composites Part B: Engineering, 2020, 200: 108358.

[49] DAI Nian-wei, ZHANG Lai-chang, ZHANG Jun-xi, CHEN Qi-meng, WU Mao-liang. Corrosion behavior of selective laser melted Ti−6Al−4V alloy in NaCl solution [J]. Corrosion Science, 2016, 102: 484−489.

[50] CHEN J R, TSAI W T. In situ corrosion monitoring of Ti−6Al−4V alloy in H_2SO_4/HCl mixed solution using electrochemical AFM [J]. Electrochimica Acta, 2011, 56(4): 1746−1751.

[51] CHEN Gang, LIU Shu-ying, HUANG Chao, MA Yuan, LI Ying, ZHANG Bai-cheng, GAO Lei, ZHANG Bo-wei, WANG Pei, QU Xuan-hui. In-situ phase transformation and corrosion behavior of TiNi via LPBF [J]. Corrosion Science, 2022, 203: 110348.

[52] AGBEDOR S O, WU Hong, REN Yao-jia, LIANG Lu-xin, YANG Dong-hui, LIU Bin, LIU Yong, BAKER I. A two-decade odyssey in fusion-based additive manufacturing of titanium alloys and composites [J]. Applied Materials Today, 2024, 39: 102242.

激光粉末床熔融 Ti−12Ni 合金的显微组织演变、力学性能及耐蚀性

黄 凯[1]，任垚嘉[1]，王清鸽[1]，刘 毅[2]，付 全[2]，李 宁[3]，Ian BAKER[4]，宋 旼[1]，吴 宏[1]

1. 中南大学 粉末冶金国家重点实验室，长沙 410083；
2. 云南贵金属实验室有限公司，昆明 650106；
3. 中南大学 湘雅医院 口腔医学中心 口腔颌面外科，长沙 410008；
4. Thayer School of Engineering, Dartmouth College, Hanover, NH 03755, USA

摘 要：通过改变工艺参数体能量密度(VED)研究了激光粉末床熔融 Ti−12Ni(质量分数，%)合金的显微组织演变、力学性能和腐蚀行为。结果表明，在 VED 为 67 J/mm^3 下制备的合金由近 β 晶粒组成。在 VED 为 133 J/mm^3 下的合金呈粗大初生 Ti_2Ni 和精细共析结构。该共析结构由 α 板条及纳米尺寸的短棒状和球形 Ti_2Ni 组成。进一步增加 VED 至 267 J/mm^3 导致共析结构变粗。分散的纳米 Ti_2Ni 具有显著的强化作用，使在 VED 为 133 J/mm^3 条件下制备的合金表现出(7.8±0.1) GPa 的纳米硬度和(1777±27) MPa 的压缩强度。然而，Ni 偏析和成形孔洞会对合金的耐蚀性产生不利影响。

关键词：Ti−12Ni 合金；激光粉末床熔融；显微组织演变；力学性能；耐蚀性

(Edited by Wei-ping CHEN)